

Friction and slip measured at the bed of an Antarctic ice stream

Thomas Hudson (✉ thomas.hudson@earth.ox.ac.uk)

University of Oxford <https://orcid.org/0000-0003-2944-883X>

Sofia-Katerina Kufner

German Research Centre for Geosciences Potsdam <https://orcid.org/0000-0002-9687-5455>

Alex Brisbane

British Antarctic Survey, Natural Environment Research Council <https://orcid.org/0000-0002-9887-7120>

Michael Kendall

University of Oxford <https://orcid.org/0000-0002-1486-3945>

Andrew Smith

British Antarctic Survey <https://orcid.org/0000-0001-8577-482X>

Richard Alley

Pennsylvania State University

Robert Arthern

N.E.R.C. British Antarctic Survey

Tavi Murray

Swansea University <https://orcid.org/0000-0001-6714-6512>

Article

Keywords:

Posted Date: January 13th, 2022

DOI: <https://doi.org/10.21203/rs.3.rs-1214097/v1>

License:  This work is licensed under a Creative Commons Attribution 4.0 International License.

[Read Full License](#)

1
2 **Friction and slip measured at the bed of an Antarctic ice stream**
3

4 T.S. Hudson^{1*}, SK Kufner², A.M. Brisbourne², JM Kendall¹, A.M. Smith², R.B. Alley³, R.J.
5 Arthern², T. Murray⁴

6 **Affiliations:**

7
8 ¹Department of Earth Sciences, University of Oxford; 3 South Parks Rd, Oxford, OX1 3AN,
9 UK

10
11 ²UKRI British Antarctic Survey; High Cross, Madingley Rd, Cambridge, CB3 0ET, UK

12
13 ³Department of Geosciences, and Earth and Environmental Systems Institute, Pennsylvania
14 State University, University Park, PA 16802, USA

15
16 ⁴Department of Geography, Swansea University, Swansea, Singleton Park, Swansea, SA2
17 8PP, UK

18
19 *Corresponding author email address: thomas.hudson@earth.ox.ac.uk

20
21 **Abstract:**

22 The slip of glaciers over the underlying bed is the dominant mechanism governing the migration
23 of ice from land into the oceans, contributing to sea-level rise. Yet glacier slip remains poorly
24 understood or constrained by observations. Here we observe both frictional shear-stress and slip
25 at the bed of an ice stream, using 100,000 repetitive stick-slip icequakes from Rutford Ice
26 Stream, Antarctica. Basal shear-stresses and slip-rates vary from 10^4 to $10^7 Pa$ and 0.2 to
27 $1.5 m day^{-1}$, respectively. Friction and slip vary temporally over the order of hours and
28 spatially over 10s of meters, caused by corresponding variations in ice-bed interface material and
29 effective-normal-stress. Our findings also suggest that the bed is substantially more complex
30 than currently assumed in ice stream models and that basal effective-normal-stresses may be
31 significantly higher than previously thought. The observations also provide previously
32 unresolved constraint of the basal boundary conditions of ice dynamics models. This is critical
33 for constraining the primary contribution of ice mass loss in Antarctica, and hence the endeavor
34 to reduce uncertainty in sea-level rise projections.

37 **Main Text:**

38 Glacier slip is the primary mechanism governing the migration of ice from land into the oceans,
39 providing a major contribution to sea-level rise^{1,2}. Friction at the bed of a glacier fundamentally
40 limits the speed at which the ice can slip. This friction is controlled by a number of factors,
41 including bed material, the presence of debris in basal ice, and hydrological systems that
42 modulate effective-normal-stresses. However, basal friction and slip remain poorly understood or
43 constrained by observations^{1,3,5}. Such observational constraint of friction and slip is critical for
44 the verification of ice-bed boundary condition assumptions in ice dynamics models, which are
45 required to reduce uncertainty in corresponding sea-level rise projections^{4,6,7}.

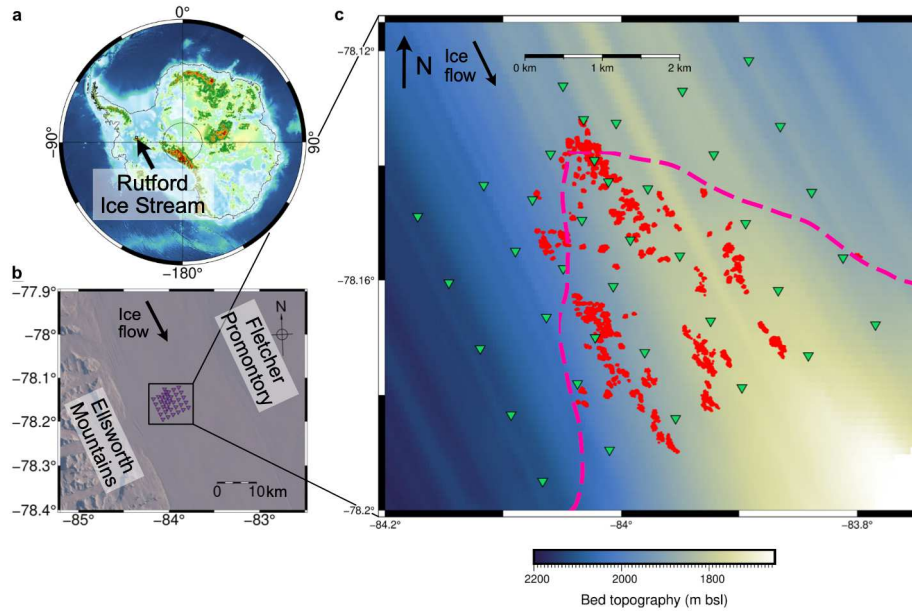
46

47 Previous contributions to address this critical observational void come from laboratory-based
48 experiments^{8–13} geophysical studies^{14–23}, and borehole measurements^{24,25}. However, to date there
49 have been challenges with such approaches. Laboratory experiments provide insight into
50 fundamental physical properties of the bed material (till)¹⁰ and ice-bed interface interactions¹²
51 but are limited by scale and the diversity of natural glacier beds. Geophysical studies have
52 measured the in-situ bed strength, but with sparse spatial and temporal resolution¹⁴. Borehole
53 measurements of slip are not only sparse, but have not been accompanied by measurements of
54 shear-stress, making quantitative interpretations difficult. The ice streams and outlet glaciers that
55 contribute the majority of ice flux into the oceans likely have active, spatially- and temporally-
56 varying hydrological systems^{26,27}, perturbing basal friction and slip over short time- and length-
57 scales. An observational void therefore remains.

58

59 Here we address this observational void by using icequakes to provide the first spatially-mapped,
60 in-situ observations of both frictional drag and slip-rate at the bed of an ice stream. These
61 icequakes are generated by the sudden release of strain at or near the ice-bed interface. The
62 dataset analyzed comprises 100,000 icequakes²⁸ from Rutford Ice Stream (RIS), Antarctica (see
63 Fig. 1). The icequakes originate approximately at the center of the ice stream, where the
64 dominant source of drag is postulated to originate from the bed rather than from the shear
65 margins. These icequakes nucleate in clusters that are highly repetitive (see Extended Data Fig.
66 1), with near-constant inter-event times of the order of 100s of seconds and icequakes clusters
67 active for hours to days²⁸. These icequakes are inferred to be at the bed from: their hypocentral
68 depths; the consistent flow- and bed- parallel orientation of their double-couple focal mechanism
69 slip-vectors; and full-waveform modelling a typical RIS icequake source^{20,28–30}. The tight spatial
70 clustering and repetitive nature motivate our use of a rate-and-state friction law in combination
71 with icequake observations to investigate the glacier sliding process. This rate-and-state friction
72 law³¹ also enables the calculation of other basal parameters including bed shear moduli and
73 insight into the modulation of glaciological effective-normal-pressures.

74



75

76 **Fig. 1. Seismic network and icequake data at Rutford Ice Stream, Antarctica.** (a) Location
 77 of Rutford Ice Stream (RIS) relative to the Antarctic continent. Topography is from Bedmap2³².
 78 (b) Map of network with respect to RIS shear-margins. (c) Map of the experiment and icequake
 79 data at Rutford Ice Stream, from November 2018 to February 2019. Red scatter points show
 80 icequake locations. All icequakes are approximately at ice stream bed²⁸. Green inverted triangles
 81 show geophone locations. Bed topography data are from the literature³³. Pink dashed line
 82 indicates a bed-character boundary from the literature³³.

83

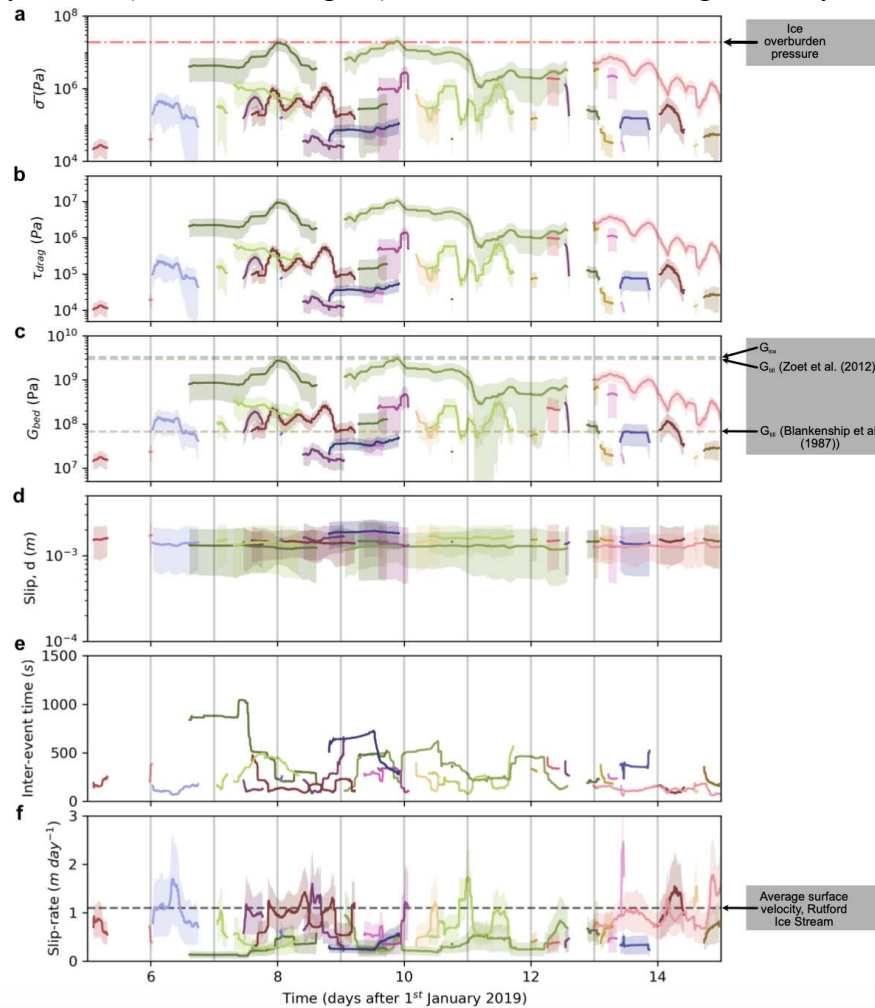
84 Results

85 Observed ice-bed friction and slip-rate

86 The icequake source properties and inter-event times are used in combination with a rate-and-
 87 state friction law to calculate: fault effective-normal-stress ($\bar{\sigma}$); total frictional shear-stress, or
 88 drag per unit area (τ); shear-modulus (G_{bed}); slip (d); and slip-rate (v_{slip}) at the bed of RIS. Fig.
 89 2 shows these results for a representative subset of icequake clusters. Fault effective-normal-
 90 stress, shear-stress and shear-modulus (Fig. 2a-c) vary by orders of magnitude between clusters,
 91 even after accounting for uncertainty. However, these parameters are all confined within
 92 expected physical limits. Effective-normal-stresses remain below the maximum ice overburden
 93 pressure, which is the upper possible limit for the average effective-normal-stress over the entire
 94 fault. The observed shear-stress ranges from $\sim 10^4$ to 10^7 Pa. If the icequake cluster locations,
 95 or sticky-spots, contribute more drag than the surrounding bed, then sticky-spot shear-stresses
 96 could theoretically have a much higher limit than the average bed shear-stress. Although bed
 97 shear moduli vary significantly between clusters, the majority of the clusters' shear moduli agree
 98 with one of the only previous seismically-derived in-situ measurements, 70 MPa, from Whillans
 99 Ice Stream¹⁴. Additionally, measurements do not exceed the shear-modulus of ice.

100

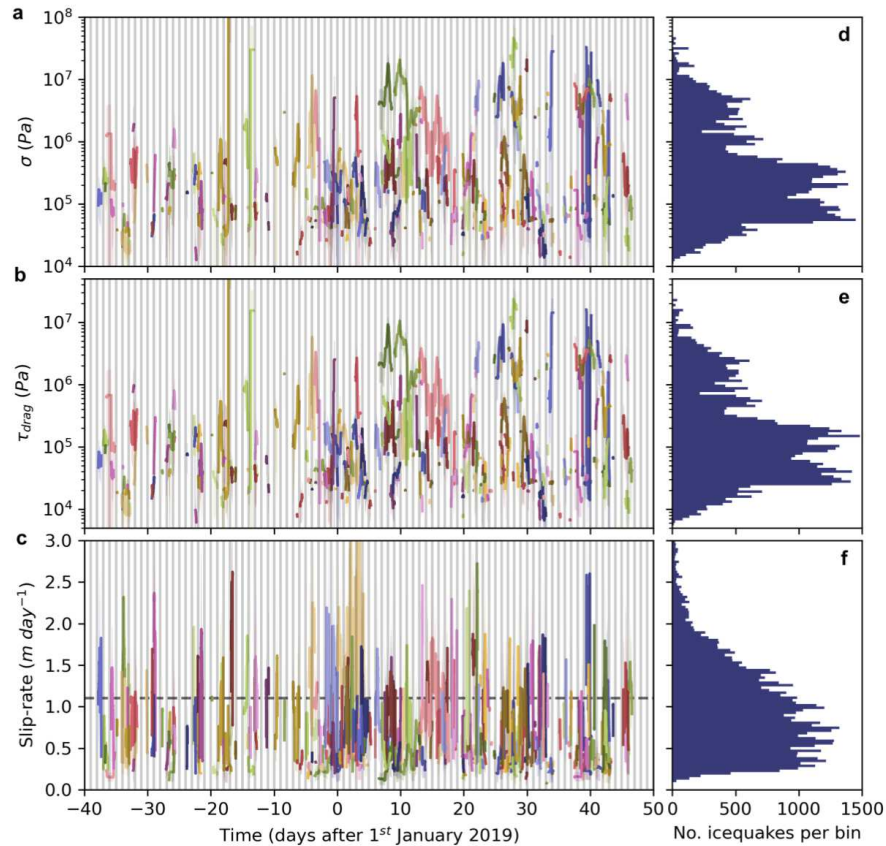
101 Slip-rates show smaller variations in amplitude, from ~ 0.2 to 1.5 m day^{-1} , but have higher
 102 associated uncertainties due to their dependence on both shear-modulus and fault-area. While a
 103 number of clusters exhibit time-averaged slip-rates approximately equal to the steady-state
 104 surface velocity of RIS (dashed line, Fig. 2f)³⁴, other clusters have significantly lower slip-rates.



105
 106 **Fig. 2. All icequake-derived basal sliding parameters through time.** Data are a subset of
 107 icequake clusters over the period of 5th to 15th January 2019. Each colored line represents an
 108 individual icequake cluster. Uncertainties are shown by shaded regions. (a) Effective-normal-
 109 stress. Red dashed-dotted line indicates the maximum possible ice overburden pressure. (b) Total
 110 frictional basal shear-stress. (c) Bed shear-modulus. Previous estimates from literature are
 111 indicated by the dashed lines^{14,15}. (d) Slip associated with individual icequakes. (e) Inter-event
 112 time between icequakes in a cluster. (f) Equivalent daily slip-rate calculated from the slip and
 113 inter-event times in (d) and (e). All data is smoothed by applying a 100-event moving-average
 114 window. All uncertainties are estimated using calculus-derived uncertainty propagation methods.
 115 Sensitivity analysis of the rate-and-state model is shown in Extended Data Fig. 5.

116
 117 Fig. 3a-c show the variation in effective-normal-stress, shear-stress and slip-rate for the entire
 118 experiment duration. Histograms of the stress and slip-rate distributions are shown in Fig. 3d-f.
 119 The normal and shear-stress histograms show a bimodal distribution, with more than two thirds
 120 of the icequakes having effective-normal-stresses lower than $\sim 5 \times 10^5 \text{ Pa}$ and shear-stresses

121 lower than 2×10^5 Pa. Conversely, the slip-rates exhibit a unimodal distribution, tailing off
 122 below 0.2 m day^{-1} and above 1.5 m day^{-1} .



123

124 **Fig. 3. Basal effective-normal-stress, shear-stress and slip-rate for the entire experiment.**
 125 Colored lines represent individual icequake clusters. (a) Effective-normal-stress on the fault. (b)
 126 Shear-stress through time. (c) Slip-rate through time. (d) to (f) Histograms of the respective time-
 127 series data in (a) to (c). Uncertainties in (a) to (c) are given by the shaded regions. Other labels as
 128 in Fig. 2. Uncertainties are as defined in Fig. 2.

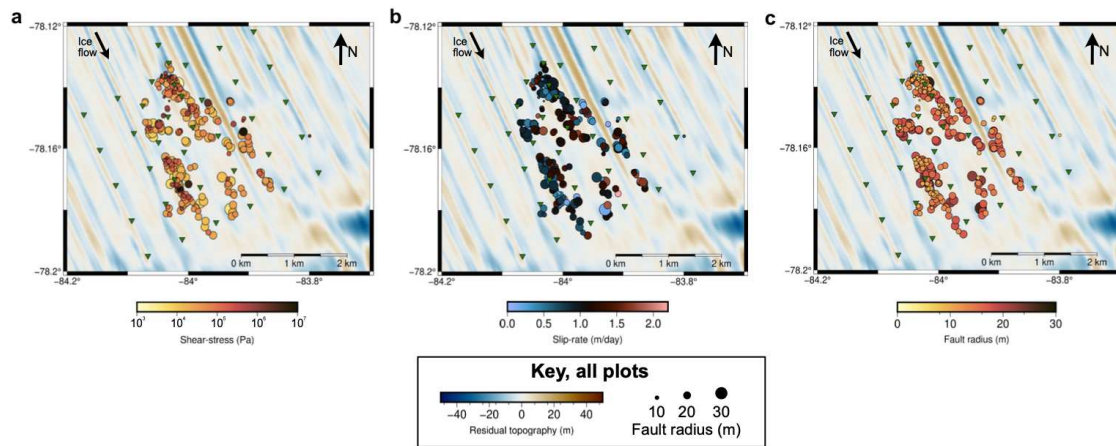
129

130 Individual icequake clusters switch on and off, being active for the order of hours to days (see
 131 Fig. 2). Within single clusters, bed friction and slip are modulated by signals with dominant
 132 periods of ~ 6 to 12 hours (see Fig. 2). However, although this alludes to tidal modulation of
 133 basal friction, and indeed surface velocities are known to be modulated by tidal frequencies^{34,35},
 134 we cannot decipher a clear relationship between tidal signals propagated 40 km upstream from
 135 RIS's grounding line and our signals²⁸. We therefore do not discuss any link with tidal signals
 136 further.

137

138 The spatial distribution of average basal shear-stress, slip-rate and fault radius for each cluster
 139 over a 7×6 km region are shown in Fig. 4. Shear-stresses are largest at the clusters farthest
 140 upstream, approximately where the bed properties are inferred to transition from unconsolidated
 141 to consolidated till³³ (pink dashed-line, Fig. 1) and where the bed has shorter wavelength

142 topography than upstream that likely inhibits ice flow. Average slip-rate is spatially consistent
 143 across all clusters. This is expected, as our study site is located near the center of the ice stream,
 144 with no spatial variation in surface slip-rate³⁴. Fault radius, defining the area of an icequake
 145 cluster sticky-spot is also measured (see Fig. 4c). Fault radii indicate that individual seismically
 146 active sticky-spots have areas < 2800 m². Only a small number of sticky-spots are active at any
 147 instant. This suggests that regions of sufficiently high basal friction to generate seismicity are
 148 confined to the minority of the bed at a given point in time, yet invoke significant basal drag.
 149 Aseismic regions between icequake clusters likely also contribute to the basal drag, presumably
 150 providing the dominant source of aseismic drag upstream of the unconsolidated-consolidated
 151 sediment boundary (pink dashed line, Fig. 1).



152

153 **Fig. 4. Spatial variability in average basal shear-stress, slip-rate and fault radius for the**
 154 **clusters.** (a) Average shear-stress for the clusters. (b) Average slip-rate for the clusters. (c)
 155 Average fault radius for the clusters. Residual topography data is from ground-penetrating
 156 radar³³. Size of scatter points indicates fault radius. Green inverted triangles indicate the
 157 locations of the network of receivers used in this study.

158

159 Discussion

160 Frictional shear-stress and slip-rate

161 The most important, immediate finding of this work is the ability to observe in-situ frictional
 162 shear-stress and slip-rate, the two critical parameters for constraining the basal drag boundary
 163 conditions of ice dynamics models. Our approach could be applied to any glacier that generates
 164 icequakes. Most fast-moving glaciers likely generate such icequakes, with the majority of
 165 glaciers on which seismometers have been deployed exhibiting at least some basal
 166 seismicity^{16,28,36-44}. Seismic tremor associated with sliding can also occur^{19,45}, thought to initiate
 167 at the boundary between the conditionally-stable and unstable regimes of the rate-and-state
 168 friction model^{19,31}. Indeed, the premise of this study was inspired by such observations¹⁹.
 169 However, due to the inability to extract both corner frequency and inter-event time information
 170 from tremor, it cannot be used to measure shear-stress and slip using our approach.

171

172 Our confidence in the frictional shear-stress and slip-rate measurements is founded partially on
 173 the uncertainty amplitudes, but also fundamentally on the agreement between the observed basal
 174 slip-rates and GNSS-derived surface displacement³⁴. This agreement validates assumptions of
 175 slip-dominant rather than deformation-dominant flow at RIS and the use of a rate-and-state
 176 model and assumptions of the icequake source properties. The small discrepancy between the
 177 surface and basal slip-rates is primarily due to uncertainty, except for a minority of particularly
 178 sticky-spots. These sticky-spots exhibit particularly strong frictional drag that significantly
 179 inhibits local ice flow, albeit for short durations of the order of hours to days.

180
 181 Observed basal shear-stresses are of the order of 10^4 to 10^7 Pa, acting at sticky-spots with
 182 diameters of the order of 10 to 60 m (see Fig. 4). Basal shear-stresses of the order 10^5 Pa are
 183 typical values used in ice dynamics models⁴⁶ and laboratory experiments⁸ for RIS's surface slip-
 184 rate of ~ 400 m/yr³⁴. Basal shear-stresses of 10^6 to 10^7 Pa might initially appear inconsistently
 185 high compared to models and experiments⁴⁷. However, these high friction sticky-spots are
 186 spatially small compared to the total bed area. Our results therefore imply that certain icequake
 187 clusters accommodate a considerable proportion of the total basal drag.

188 189 **Icequake generation mechanisms**

190 We propose that the icequakes are generated by at least one of two mechanisms, or sliding
 191 regimes. The presence of two sliding regimes is motivated by the physical system and the
 192 bimodal distributions observed in Fig. 3d,e. The regimes (see Fig. 5) are: regime I, rock-on-rock
 193 friction between ice-entrained clasts and bedrock at the fault interface; and regime II, where
 194 clasts plough through till, with failure accommodated by a till-on-till fault interface. Clasts are
 195 pieces of rock partially entrained into the ice (see Fig. 5). The presence of such clasts is
 196 discussed in the literature^{8,12,13,48,49}. The motivations for these clast-based icequake models are
 197 that they can explain the rate-weakening friction required to generate icequakes¹³, that clasts are
 198 required to generate icequakes in laboratory environments¹², and that such icequakes likely
 199 originate within one seismic wavelength of the ice-bed interface²⁰. We suggest that the highest
 200 effective-normal-stress icequakes exhibit regime I sliding, since this regime allows for the
 201 average effective-normal-stress over the entire fault-area to be concentrated over much smaller
 202 clast-bedrock contact areas. Similarly, we postulate that the lower effective-normal-stress
 203 icequakes are associated with regime II sliding, although we cannot rule out that all icequakes
 204 are generated via regime I.

205 206 **Effective normal-stress vs. effective fluid pressure**

207 Our results imply significant temporal variation in basal effective-normal-stress. Such increases
 208 and decreases in effective-normal-stress are inferred to be caused by corresponding decreases
 209 and increases in basal water pressure^{16,50,51}. However, while the icequake-derived effective-
 210 normal-stresses, $\bar{\sigma}$, averaged over the entire fault are equivalent to the average glaciological
 211 effective pressure, $P_{eff} = P_{ice\ overburden} - P_{water}$, within that same fault-area, asperities and
 212 bed heterogeneity on length-scales shorter than the fault diameter could significantly perturb
 213 local effective-normal-pressure. Although all our measured effective-normal-stresses remain
 214 below the ice overburden pressure, current hydrological models cannot reconcile glaciological
 215 effective pressures greater than ~ 0.5 MPa for expected till porosities. Sparse observations of

216 effective-normal-pressures at RIS from borehole measurements find $P_{eff} \approx 0.2 \text{ MPa}$ ⁴⁹, although
 217 till acoustic impedance measurements at RIS suggest that dewatering is possible²³. Dewatered till
 218 would imply $P_{eff} = P_{ice\ overburden}$. Our highest observed effective-normal-stresses therefore
 219 suggest either: that our understanding of bed characteristics and associated physical models may
 220 have to be revisited, at the very least for RIS; or that the rate-and-state model does not
 221 adequately describe icequake physics.

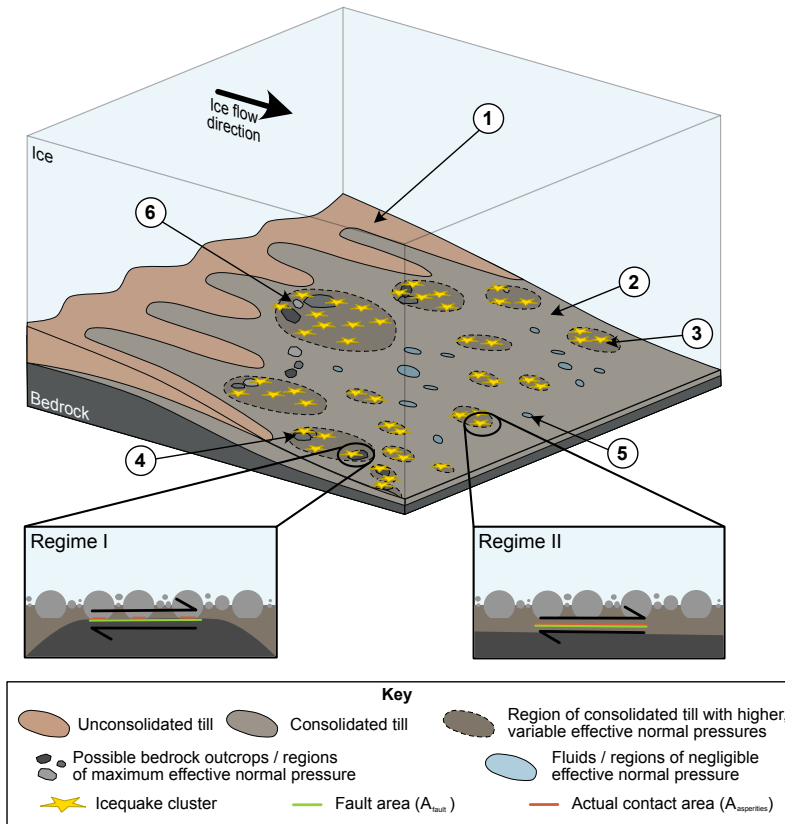
222
 223 We suggest three possible explanations for resolving the discrepancy between observed and
 224 theoretical maximum effective-normal-stresses. Firstly, prominent bedrock outcrops could
 225 significantly inhibit ice flow, allowing stoss-side effective-normal-stresses of the order of at least
 226 1 MPa to develop⁵². A second explanation again lies with bedrock outcrops, whereby
 227 impermeable bedrock might inhibit the transport of fluids, facilitating dewatered regions. A third
 228 explanation is that till porosities are far lower than conceived in current models of bed properties,
 229 possibly supported by till impedance measurements²³. These suggestions are not exhaustive. We
 230 only suggest here that our results motivate new models to explain such observations.

231
 232 If effective-normal-stresses are related to P_{eff} at sticky-spots, then they provide an observational
 233 foundation for calibrating basal-fluid-pressures assumed in: laboratory-experiments⁸; ice
 234 dynamics models⁴⁶; and glacier basal hydrology and tidal forcing^{34,35}.

235 **Enhanced knowledge of Rutford Ice Stream bed conditions**

236
 237 The considerable variation in bed properties observed at RIS are presented as an example of the
 238 enhanced knowledge of the bed properties that our approach provides. Firstly, for the
 239 unconsolidated till (label 1, Fig. 5) and much of the consolidated till (label 2, Fig. 5), the
 240 effective-normal-stresses are too low to generate the unstable stick-slip conditions required for
 241 icequake nucleation. Within consolidated till regions (label 2, Fig. 5), there are small zones that
 242 become seismically active if the effective-normal-stress is sufficiently high (label 3, Fig. 5).
 243 These sticky-spots turn on and off, modulated by changes in effective-normal-stress, bed strength
 244 and bed material.

245
 246 Frictional shear-stress at an individual sticky-spot can vary temporally by up to an order of
 247 magnitude and spatially by several orders of magnitude. This variation occurs over the order of
 248 hours and 100s meters. This implies that there are both till and bedrock outcrops, combined with
 249 an active hydrological system or permeable bed capable of such variable spatial and temporal
 250 variations in basal fluid pressure. The regions exhibiting the highest shear-stresses are at the
 251 upstream edges of local topographic highs near the unconsolidated-consolidated bed boundary
 252 (label 6, Fig. 5). This is likely because resistive stresses of these materially stronger, topographic
 253 highs can accommodate more basal drag. Some regions of consolidated till might contain
 254 pockets of melt water (label 5, Fig. 5). However, we cannot observe such a phenomenon
 255 seismically as these patches would have an approximately zero shear-modulus.



257

258 **Fig. 5. Schematic diagram summarizing the findings of this study in relation to basal**
 259 **friction and slip with bed characteristics.** Bed properties are labelled in the legend. Numbered
 260 points are referred to in the text. Note that features not to scale, but arranged approximately
 261 according to spatial trends in Fig. 4. Regime I and regime II are shown schematically, with
 262 regime I being clast-on-rock icequake slip behavior and regime II being till-on-till slip behavior.

263

264 **Wider implications**

265 Our results show that much of the basal drag at an ice stream can be accommodated within small
 266 zones of significantly higher-than-average friction. This could have a profound impact on how
 267 sliding is formulated in ice dynamics models. However, although friction varies significantly,
 268 average basal slip-rates remain predominantly stable at RIS. This is encouraging for current
 269 modelling efforts since if the temporally- and spatially- averaged slip-rates are approximately
 270 constant, then perhaps such models are not required to be sensitive to small-scale, rapid
 271 variations in bed friction. Our observations quantify the highly variable bed properties over a
 272 sufficient duration required to test such a hypothesis.

273

274 Another important question to address is how our approach could be implemented at ice sheet
 275 scale. One could deploy temporary seismic arrays on important ice streams and outlet glaciers
 276 for short durations. A number of targeted deployments would allow verification of the link
 277 between surface- and basal- velocity at ice sheet scales².

278

279 A further question that this study raises is could a rate-and-state friction model used for the
 280 icequake sliding analysis also be used as a mathematical basis for informing sliding laws used in
 281 ice dynamics models more generally. Such a model was recently proposed to describe surging
 282 glacier behavior⁵³ and has been validated at laboratory scale^{12,13}. The rate-and-state model meets
 283 the conditional stability requirement, not allowing runaway acceleration of a glacier. A more
 284 comprehensive comparison to sliding laws for deformable beds, showing agreement for surface
 285 velocities > 100 m/yr, is provided in the supplementary text.

286
 287 Finally, these icequakes observations can aid the understanding of earthquake mechanics more
 288 generally. Even the smallest magnitude icequakes ($M_w \approx -1.5$) have high signal-to-noise-ratios,
 289 and so could elucidate any lower limits on the fundamental size of earthquake nucleation for
 290 given fault properties^{54–56}. Additionally, icequakes in this study have stress-drops that vary with
 291 magnitude, contrary to magnitude-invariant stress-drops observed for larger earthquakes⁵⁷.

292
 293 Our findings show that icequakes can provide the critical observations required to constrain the
 294 highly variable friction at the bed of an Antarctic ice stream. Applying such observational
 295 constraint to ice dynamics models would reduce uncertainty in corresponding sea-level rise
 296 projections.

297 298 References

- 299 1. Morlighem, M. et al. Spatial patterns of basal drag inferred using control methods from a full-
 300 Stokes and simpler models for Pine Island Glacier, West Antarctica. *Geophys. Res. Lett.* 37, 1–6
 301 (2010).
- 302 2. Rignot, E., Mouginot, J. & Scheuchl, B. Ice Flow of the Antarctic Ice Sheet. *Science* (80-.). 333,
 303 1427–1430 (2011).
- 304 3. Ritz, C. et al. Potential sea-level rise from Antarctic ice-sheet instability constrained by
 305 observations. *Nature* 528, 115–118 (2015).
- 306 4. Tsai, V. C., Stewart, A. L. & Thompson, A. F. Marine ice-sheet profiles and stability under
 307 Coulomb basal conditions. *J. Glaciol.* 61, 205–215 (2015).
- 308 5. Joughin, I., Smith, B. E. & Schoof, C. G. Regularized Coulomb Friction Laws for Ice Sheet
 309 Sliding: Application to Pine Island Glacier, Antarctica. *Geophys. Res. Lett.* 46, 4764–4771 (2019).
- 310 6. Oppenheimer, M. et al. Sea Level Rise and Implications for Low-Lying Islands, Coasts and
 311 Communities. IPCC Spec. Rep. Ocean Cryosph. a Chang. Clim. 321–445 (2019).
- 312 7. Schlegel, N. J. et al. Exploration of Antarctic Ice Sheet 100-year contribution to sea level rise and
 313 associated model uncertainties using the ISSM framework. *Cryosphere* 12, 3511–3534 (2018).
- 314 8. Zoet, L. K. & Iverson, N. R. A slip law for glaciers on deformable beds. *Science* (80-.). 368, 76–
 315 78 (2020).
- 316 9. Iverson, N., Baker, R., Hooke, R., Hanson, B. & Jansson, P. Coupling between a glacier and a soft
 317 bed: I. A relation between effective pressure and local shear stress determined from till elasticity.
 318 *J. Glaciol.* 45, 31–40 (1999).
- 319 10. Tulaczyk, S., Kamb, W. B. & Engelhart, H. F. Basal mechanics of Ice Stream B, west Antarctica:
 320 1. Till mechanics. *J. Geophys. Researh* 105, 463–481 (2000).
- 321 11. Leeman, J. R., Valdez, R. D., Alley, R. B., Anandkrishnan, S. & Saffer, D. M. Mechanical and
 322 hydrologic properties of Whillans Ice Stream till: Implications for basal strength and stick-slip
 323 failure. *J. Geophys. Res. Earth Surf.* 121, 1–17 (2016).
- 324 12. Zoet, L. K. et al. Application of Constitutive Friction Laws to Glacier Seismicity. *Geophys. Res.*
 325 *Lett.* 47, 1–9 (2020).

- 326 13. Lipovsky, B. P. et al. Glacier sliding, seismicity and sediment entrainment. *Ann. Glaciol.* 60, 182–
327 192 (2019).
- 328 14. Blankenship, D. D., Bentley, C. R., Rooney, S. T. & Alley, R. B. Till beneath Ice Stream B 1.
329 Properties derived from seismic travel times. *J. Geophys. Res.* 92, 8903–8911 (1987).
- 330 15. Zoet, L. K., Anandakrishnan, S., Alley, R. B., Nyblade, A. A. & Wiens, D. A. Motion of an
331 Antarctic glacier by repeated tidally modulated earthquakes. *Nat. Geosci.* 5, 623–626 (2012).
- 332 16. Gräff, D. & Walter, F. Changing friction at the base of an Alpine glacier. *Sci. Rep.* 11, 1–10
333 (2021).
- 334 17. Winberry, J. P., Anandakrishnan, S., Alley, R. B., Bindschadler, R. A. & King, M. A. Basal
335 mechanics of ice streams: Insights from the stick-slip motion of Whillans Ice Stream, West
336 Antarctica. *J. Geophys. Res.* 114, 1–11 (2009).
- 337 18. Anandakrishnan, S. & Bentley, C. R. Micro-earthquakes beneath ice streams B and C, West
338 Antarctica: observations and implications. *J. Glaciol.* 39, 455–462 (1993).
- 339 19. Lipovsky, B. P. & Dunham, E. M. Tremor during ice-stream stick slip. *Cryosphere* 10, 385–399
340 (2016).
- 341 20. Hudson, T. S. et al. Icequake Source Mechanisms for Studying Glacial Sliding. *J. Geophys. Res.*
342 *Earth Surf.* 125, (2020).
- 343 21. Wiens, D. A., Anandakrishnan, S., Winberry, J. P. & King, M. A. Simultaneous teleseismic and
344 geodetic observations of the stick-slip motion of an Antarctic ice stream. *Nature* 453, 770–774
345 (2008).
- 346 22. Barcheck, C. G., Tulaczyk, S., Schwartz, S. Y., Walter, J. I. & Winberry, J. P. Implications of
347 basal micro-earthquakes and tremor for ice stream mechanics: Stick-slip basal sliding and till
348 erosion. *Earth Planet. Sci. Lett.* 486, 54–60 (2018).
- 349 23. Smith, A. M. & Murray, T. Bedform topography and basal conditions beneath a fast-flowing West
350 Antarctic ice stream. *Quat. Sci. Rev.* 28, 584–596 (2009).
- 351 24. Engelhardt, H. Basal sliding of Ice Stream B, West Antarctica. *J. Glaciol.* 44, 223–230 (1998).
- 352 25. Truffer, M., Harrison, W. D. & Echelmeyer, K. A. Glacier motion dominated by processes deep in
353 underlying till. *J. Glaciol.* 46, 213–221 (2000).
- 354 26. Rosier, S. H. R., Gudmundsson, G. H. & Green, J. A. M. Temporal variations in the flow of a
355 large Antarctic ice stream controlled by tidally induced changes in the subglacial water system.
356 *Cryosph.* 9, 1649–1661 (2015).
- 357 27. Damsgaard, A. et al. Ice flow dynamics forced by water pressure variations in subglacial granular
358 beds. *Geophys. Res. Lett.* 43, 12,165–12,173 (2016).
- 359 28. Kufner, S. et al. Not all Icequakes are Created Equal: Basal Icequakes Suggest Diverse Bed
360 Deformation Mechanisms at Rutford Ice Stream, West Antarctica. *J. Geophys. Res. Earth Surf.*
361 126, (2021).
- 362 29. Smith, E. C., Smith, A. M., White, R. S., Brisbourne, A. M. & Pritchard, H. D. Mapping the ice-
363 bed interface characteristics of Rutford Ice Stream, West Antarctica, using microseismicity. *J.*
364 *Geophys. Res. Earth Surf.* 120, 1881–1894 (2015).
- 365 30. Smith, A. M. Microearthquakes and subglacial conditions. *Geophys. Res. Lett.* 33, 1–5 (2006).
- 366 31. Scholz, C. H. Earthquakes and friction laws. *Nature* 391, 37–42 (1998).
- 367 32. Fretwell, P. et al. Bedmap2: Improved ice bed, surface and thickness datasets for Antarctica.
368 *Cryosphere* 7, 375–393 (2013).
- 369 33. King, E. C., Pritchard, H. D. & Smith, A. M. Subglacial landforms beneath Rutford Ice Stream,
370 Antarctica: detailed bed topography from ice-penetrating radar. *Earth Syst. Sci. Data* 8, 151–158
371 (2016).
- 372 34. Minchew, B. M., Simons, M., Riel, B. & Milillo, P. Tidally induced variations in vertical and
373 horizontal motion on Rutford Ice Stream, West Antarctica, inferred from remotely sensed
374 observations. *J. Geophys. Res. Earth Surf.* 122, 167–190 (2017).
- 375 35. Rosier, S. H. R., Gudmundsson, G. H. & Green, J. A. M. Temporal variations in the flow of a
376 large Antarctic ice stream controlled by tidally induced changes in the subglacial water system.
377 *Cryosphere* 9, 1649–1661 (2015).

- 378 36. Stuart, G., Murray, T., Brisbourne, A., Styles, P. & Toon, S. Seismic emissions from a surging
379 glacier: Bakaninbreen, Svalbard. *Ann. Glaciol.* 42, 151–157 (2005).
- 380 37. Walter, F., Deichmann, N. & Funk, M. Basal icequakes during changing subglacial water
381 pressures beneath Gornergletscher, Switzerland. *Mitteilungen der Versuchsanstalt für Wasserbau,
382 Hydrol. und Glaziologie an der Eidgenoss. Tech. Hochschule Zurich* 54, 511–521 (2008).
- 383 38. Hudson, T. S., Smith, J., Brisbourne, A. & White, R. Automated detection of basal icequakes and
384 discrimination from surface crevassing. *Ann. Glaciol.* 60, 1–11 (2019).
- 385 39. Roeoesli, C., Helmstetter, A., Walter, F. & Kissling, E. Meltwater influences on deep stick-slip
386 icequakes near the base of the Greenland Ice Sheet. *J. Geophys. Res. Earth Surf.* 1–18 (2016)
387 doi:10.1002/2015JF003601.
- 388 40. McBrearty, I. W., Zoet, L. K. & Anandakrishnan, S. Basal seismicity of the Northeast Greenland
389 Ice Stream. *J. Glaciol.* 1–17 (2020) doi:10.1017/jog.2020.17.
- 390 41. Bindschadler, R. A., King, M. A., Alley, R. B., Anandakrishnan, S. & Padman, L. Tidally
391 controlled stick-slip discharge of a West Antarctic ice stream. *Science* (80-.). 301, 1087–1089
392 (2003).
- 393 42. Anandakrishnan, S. & Alley, R. B. Ice Stream C, Antarctica, sticky-spots detected by
394 microearthquake monitoring. *Ann. Glaciol.* 20, 183–186 (1994).
- 395 43. Deichmann, N. et al. Evidence for deep icequakes in an Alpine glacier. *Ann. Glaciol.* 31, 85–90
396 (2000).
- 397 44. Köhler, A., Maupin, V., Nuth, C. & Pelt, W. V. A. N. Characterization of seasonal glacial
398 seismicity from a single-station on-ice record at Holtedahlfonna, Svalbard. 1–14 (2019)
399 doi:10.1017/aog.2019.15.
- 400 45. Winberry, J. P., Anandakrishnan, S., Wiens, D. A. & Alley, R. B. Nucleation and seismic tremor
401 associated with the glacial earthquakes of Whillans Ice Stream, Antarctica. *Geophys. Res. Lett.* 40,
402 312–315 (2013).
- 403 46. Cornford, S. L. et al. Results of the third Marine Ice Sheet Model Intercomparison Project
404 (MISMIP+). *Cryosphere* 14, 2283–2301 (2020).
- 405 47. Ranganathan, M., Minchew, B., Meyer, C. R. & Gudmundsson, G. H. A new approach to inferring
406 basal drag and ice rheology in ice streams, with applications to West Antarctic Ice Streams. *J.
407 Glaciol.* 67, 229–242 (2021).
- 408 48. Hallet, B. A theoretical model of glacier abrasion. *J. Glaciol.* 23, 39–50 (1979).
- 409 49. Smith, A. M. et al. Ice stream subglacial access for ice-sheet history and fast ice flow: The
410 BEAMISH Project on Rutford Ice Stream, West Antarctica and initial results on basal conditions.
411 *Ann. Glaciol.* (2020) doi:10.1017/aog.2020.82.
- 412 50. Sugiyama, S. & Gudmundsson, G. H. Short-term variations in glacier flow controlled by
413 subglacial water pressure at Lauteraargletscher, Bernese Alps, Switzerland. *J. Glaciol.* 50, 353–
414 362 (2004).
- 415 51. Bindschadler, R. The importance of pressurized subglacial water in separation and sliding at the
416 glacier bed. *J. Glaciol.* 29, 3–19 (1983).
- 417 52. Alley, R. B. et al. Bedforms of Thwaites Glacier, West Antarctica: Character and Origin. *J.
418 Geophys. Res. Earth Surf.* (in Rev. (2021) doi:10.1029/2021JF006339).
- 419 53. Thøgersen, K., Gilbert, A., Schuler, T. V. & Malthe-Sørenssen, A. Rate-and-state friction explains
420 glacier surge propagation. *Nat. Commun.* 10, 1–8 (2019).
- 421 54. Dieterich, J. H. Earthquake nucleation on faults with rate-and state-dependent strength.
422 *Tectonophysics* 211, 115–134 (1992).
- 423 55. Cattania, C. & Segall, P. Crack Models of Repeating Earthquakes Predict Observed Moment-
424 Recurrence Scaling. *J. Geophys. Res. Solid Earth* 124, 476–503 (2019).
- 425 56. Chen, T. & Lapusta, N. Scaling of small repeating earthquakes explained by interaction of seismic
426 and aseismic slip in a rate and state fault model. *J. Geophys. Res. Solid Earth* 114, 1–12 (2009).
- 427 57. Abercrombie, R. E. Resolution and uncertainties in estimates of earthquake stress drop and energy
428 release. *Philosophical Transactions of the Royal Society A: Mathematical, Physical and
429 Engineering Sciences* vol. 379 (2021).

430
431
432
433
434
435
436
437
438
439
440
441
442
443
444
445
446
447
448
449
450
451
452
453
454
455
456
457
458
459
460
461
462
463
464

Acknowledgments:

We thank NERC British Antarctic Survey for logistics and field support, and specifically the BEAMISH field team (2018/2019). We also thank J. Hawthorne, R. Katz and S. Anandkrishnan for valuable discussions and feedback. AMB, AMS, and TM were funded by Natural Environment Research Council grants NE/G014159/1 and NE/G013187/1, Seismic instruments were provided by NERC SEIS-UK (Loans 1017 and 1111), by BAS and by the Incorporated Research Institutions for Seismology (IRIS) through the PASSCAL Instrument Center at New Mexico Tech. The facilities of the IRIS Consortium are supported by the National Science Foundation's Seismological Facilities for the Advancement of Geoscience (SAGE) Award under Cooperative Support Agreement EAR- 1851048. All the seismic data used in this analysis will be deposited on the IRIS seismological data repository. The icequake catalogue used for this analysis is available from the UK Polar Data Centre⁵⁸, with details on how this catalogue was constructed given in the peer-reviewed publication²⁸. All the fundamental code used in this study is available open source. QuakeMigrate⁵⁹ was used for icequake detection, NonLinLoc for icequake relocation⁶⁰ and SeisSrcMoment for the moment magnitude and other source parameter analysis⁶¹.

465 Methods

466 The icequake dataset

467 This study uses 100,000 icequakes at the bed of Rutford Ice Stream (RIS), Antarctica. An
 468 example of such an icequake arrival can be found in Extended Data Fig. 1. These data were
 469 collected over the period of November 2018 to February 2019. The icequakes are detected using
 470 QuakeMigrate^{38,59} and relocated using NonLinLoc⁶⁰. A full description of the detection,
 471 location and clustering analysis of this seismicity can be found in²⁸. The hypocentral depths,
 472 orientation of focal mechanisms, and full waveform modelling provide us with confidence that
 473 these icequakes are associated with sliding within one seismic wavelength (~ 10 m) of the bed
 474 ^{20,28,29}.

479 Observable parameters from stick-slip icequakes

480 Earthquake source models can be used to calculate the size of the earthquake, its duration, the
 481 fault radius and the shear-stress-drop associated with the release of seismic energy. These
 482 observable parameters are required for any analysis of frictional behavior at the bed of glaciers
 483 using icequakes. The methods we use to obtain these parameters from the icequake signals are
 484 described below.

487 *Seismic moment*

488 The seismic moment, M_0 , of an earthquake describes the energy released and is defined
 489 as⁶²,

$$491 \quad M_0 = \frac{4 \pi \rho v_i^2 r \Omega_0}{A_{rad,i} C_{free-surface}} \quad (1),$$

492 where ρ is the density of the medium at the earthquake source, v_i is the velocity of the
 493 seismic phase i (P or S), r is the hypocentre-receiver distance, Ω_0 is the long-period
 494 spectral amplitude, $A_{rad,i}$ is the amplitude of radiation of seismic phase i for the
 495 particular source-receiver azimuth and take-off angle, and $C_{free-surface}$ is the free
 496 surface correction term, which depends upon the angle of inclination of the seismic phase
 497 arrival at the surface. For this study, we assume typical ice values of $\rho = 917 \text{ kg m}^{-3}$,
 498 $v_{p,ice} = 3841 \text{ m s}^{-1}$, $v_{s,ice} = 1970 \text{ m s}^{-1}$. $A_{rad,i}$ is calculated as described in²⁰, based
 499 on the assumption that all the icequakes in this study are double-couple (DC) sources
 500 with strikes aligned with the ice flow direction. This assumption is based upon previous
 501 observations at Rutford Ice Stream^{20,28,29}. Ω_0 is calculated by fitting a Brune source
 502 model to the noise-removed spectrum of the icequake⁶³.

504 *Corner frequency*

505 The spectrum of an earthquake contains more information than just the long-period
 506 spectral amplitude. If one assumes that an earthquake's spectrum can be described by a
 507 Brune model⁶³ then one can also measure the corner frequency, f_c , of the earthquake.
 508 However, an earthquake's spectrum is also particularly sensitive to seismic attenuation.
 509

510 Seismic attenuation, often described by the quality factor, Q , reduces the amplitude of an
 511 earthquake spectrum non-linearly across all frequencies. If path attenuation is poorly
 512 constrained then it can lead to detrimental uncertainty in the measured corner frequency,
 513 as evidenced by the trade-off between Q and f_c in the Brune model ⁶³,

$$514 \quad \Omega(f) = \frac{\Omega_0 e^{-\pi f t / Q}}{1 + \left(\frac{f}{f_c}\right)^2} \quad (2),$$

515 where $\Omega(f)$ is the amplitude of the spectrum for a certain frequency f and t is the travel-
 516 time.

517
 518 To obtain an accurate measurement of corner frequency, we therefore use a linearized
 519 spectral ratios method to constrain Q . This spectral ratios method isolates the path effects
 520 from the source effects. An example of the linearized Brune model fit and the observed
 521 spectrum for an example icequake is shown in Extended Data Fig. 1c. We obtain
 522 estimates of Q from this method of the order of 200 to 800 (see Extended Data Fig. 2b),
 523 which are in agreement with other measurements for Antarctic ice ⁶⁴. This then allows
 524 Equation 1 to be fit to the earthquake spectrum with only Ω_0 and f_c as variables. We find
 525 that the icequake corner frequencies at RIS fall approximately within the range of 40-100
 526 Hz (see Extended Data Fig. 2c).

527 528 529 *Fault radius and stress-drop*

530
 531 One can estimate the fault radius, R , and stress-drop, $\Delta\tau$, of an earthquake from the
 532 corner frequency.

533
 534 The relationship between corner frequency and fault radius, R , is given by ⁶⁵,

$$535 \quad \bar{f}_c = k_i \frac{\beta}{R} \quad (3),$$

536 where \bar{f}_c is the spherically-averaged corner frequency for the earthquake, β is the shear-
 537 wave speed near the source and k_i is a constant relating the spherically-averaged corner
 538 frequencies for a specific fault model for the seismic phase i . Here, we use the fault
 539 model of ⁶⁶, which gives $k_p = 0.38$ and $k_s = 0.26$ for a rupture speed of 0.98β . We let
 540 β equal the shear velocity of ice (1970 m s^{-1} ²⁹). For clast-on-bedrock slip (Regime I,
 541 Fig. 5, main text), this is valid as rupture will propagate through the bedrock and the ice
 542 that the clasts are embedded within, with us only observing the rupture propagation
 543 through the ice. For till-on-till slip (Regime II, Fig. 5, main text), our assumption of β is
 544 likely an overestimate, resulting in an overestimate of fault radius. As the seismic
 545 properties of the till are unknown, we are limited in assigning a lower value of β for any
 546 Regime II events. We assume a symmetric circular fault for this analysis. We therefore
 547 calculate average corner frequencies for each event based on the corner frequencies
 548 observed at all receivers. The potential effects of the symmetric circular fault assumption
 549 are shown in ⁶⁷.

550
 551 The uniform stress-drop of an earthquake can then be found using the fault radius and the
 552 relationship given by ⁶⁸,

$$\Delta\tau = \frac{7}{16} \frac{M_0}{R^3} \quad (4),$$

We now have all the observable parameters required to constrain a friction model at an icequake source.

Using a rate- and state- friction law for deriving frictional shear-stress and slip from icequakes

Calculating shear-stress

Earthquakes are typically generated as the result of stick-slip frictional instabilities at a fault interface³¹. We hypothesize that icequakes associated with sliding at the bed of a glacier can be described by a similar model. For our investigation, we assume that the fault-interface is at or near (< 1 wavelength) the ice-bed interface. Schematic diagrams describing the model are given in Extended Data Fig. 3. Within this framework, we can apply the following rate- and state- friction law given by³¹,

$$\tau = \left[\mu_0 + a \ln \left(\frac{v}{v_0} \right) + b \ln \left(\frac{v_0 \theta}{\mathcal{L}} \right) \right] \bar{\sigma} \quad (5),$$

where τ is the total frictional shear-stress, μ_0 is the steady-state friction coefficient at $v = v_0$, v is the slip velocity, v_0 is a reference velocity, defined in this case to be the background slip-rate, a and b are material properties, \mathcal{L} is the characteristic slip distance over which the system returns to steady-state and renew surface contacts, and θ is the state variable. The variation of the state variable, θ , through time can be defined by the aging or the slip laws⁶⁹, given by,

$$\frac{\partial \theta}{\partial t} = 1 - \frac{v\theta}{\mathcal{L}} \quad (\text{aging law}) \quad (6),$$

$$\frac{\partial \theta}{\partial t} = -\frac{v\theta}{\mathcal{L}} \ln \left(\frac{v\theta}{\mathcal{L}} \right) \quad (\text{slip law}) \quad (7).$$

The state variable, θ , represents the characteristic contact lifetime of a fault. In order to apply the rate- and state- model to the stick-slip icequake system in a mathematically tractable way, we assume that the state variable of the system is constant over the duration of an icequake cycle, i.e. $\frac{\partial \theta}{\partial t} = 0$ through all time during a cycle. For a destructive frictional failure process, θ likely changes with time during earthquake nucleation and as the fault heals. However, for the icequake generation mechanisms proposed in this study (see Fig. 5, main text), damage at the fault interface that affects the frictional properties is likely less significant than at traditional earthquake fault interfaces. This lack of damage is evidenced to some extent by the highly repetitive nature of the icequakes^{20,28}. We assume that at least part of the icequake patch is near steady-state, or approximately at steady-state if it slips sufficiently fast. A caveat to this is that some of the icequake patch could have remained below the steady-state sliding limit, which we do not explore this here. Overall, we deem the approximation of $\frac{\partial \theta}{\partial t} = 0$ between individual icequakes as acceptable in this case. This assumption can be used to find the state variable, θ , as an expression of v , \mathcal{L} from either the aging law (Equation 6) or the slip law (Equation 7), which both yield,

594
$$\theta = \frac{\mathcal{L}}{v} \quad (8).$$

595 Equation 5 can then be reduced to a rate-dependent friction law, given by,

596
$$\tau = \left[\mu_0 + (a - b) \ln \left(\frac{v}{v_0} \right) \right] \bar{\sigma} \quad (9).$$

597 The coefficient of friction in Equation 9 can then be thought of as $\mu = \mu_0 + \Delta\mu$, where μ_0
598 is the static friction component, and the dynamic friction component, $\Delta\mu$, is given by,

599
$$\Delta\mu = (a - b) \ln \left(\frac{v}{v_0} \right) \quad (10),$$

600 which when multiplied by the effective-normal-stress, $\bar{\sigma}$, can be assumed as equal to the
601 earthquake stress-drop (see Equation 13).

602
603 One can then parametrize Equation 9 in such a way so that it can be solved for individual
604 icequakes. We take $\mu_0 = 0.4$, $a = 5 \times 10^{-3}$ and $b = 15 \times 10^{-3}$ from ¹⁹. We approximate
605 the ratio of the instantaneous sliding velocity to the reference velocity, $\frac{v}{v_0}$, as,

606
$$\frac{v}{v_0} = \frac{\left(\frac{d}{T} \right)}{\left(\frac{d}{t_{inter-event}} \right)} \quad (11),$$

607 where d is the slip associated with an event (unknown), T is the slip duration, which we
608 approximate to be equal to the inverse of the icequake corner frequency, f_c , ⁷⁰ and
609 $t_{inter-event}$ is the time between two consecutive icequakes. The correspondence of these
610 parameters to the stick-slip cycle is shown in Extended Data Fig. 3b. With this
611 parametrization, the velocity ratio then becomes,

612
$$\frac{v}{v_0} = f_c \cdot t_{inter-event} \quad (12).$$

613 Assuming that the friction at the interface is velocity-weakening and therefore unstable,
614 one can then assume that the dynamic part of Equation 9 is equal to the stress-drop
615 measured during an icequake, $\Delta\tau$ ⁷¹. One should note that this assumption implies that all
616 the dynamic stress-release during slip is accommodated seismically (see red shaded
617 region of Extended Data Fig. 3b). However, there is also frictional shear-stress present
618 that cannot be measured directly using stress-drop measurements. We also assume a
619 seismic radiation efficiency of 1, which is obviously an approximation, with the actual
620 seismic radiation efficiency unknown. Although the radiation efficiency will in reality be
621 <1 , due to thermal heating and the generation of additional surface area during abrasion,
622 fracture tip energy, and other phenomena such as off-fault cracking are likely
623 insignificant in comparison to standard earthquakes ⁷², so we deem our first-order
624 approximation as reasonable in this case. For tectonic earthquakes, the seismic radiation
625 efficiency typically might be of the order of 0.1 (for example, see ⁷³). If the icequake
626 seismic radiation efficiencies were similarly low, then this would be approximately
627 equivalent to reducing the magnitude of M_0 by a factor of 10. Sensitivity analysis in the
628 supplementary text suggests that such a reduction in M_0 would reduce the shear-stress, τ ,
629 by an order of magnitude, but the slip velocity, v_{slip} , would only be reduced by a factor
630 of 3. Assuming velocity-weakening friction and a radiation efficiency of one results in
631 the definition of the effective-normal-stress at the fault interface, given by,

632

$$\bar{\sigma} = \frac{\Delta\tau}{(a-b)\ln\left(\frac{v}{v_0}\right)} \quad (13).$$

633

Once we know the effective-normal-stress, $\bar{\sigma}$, we can find the overall shear-stress on the fault, τ , from Equation 9.

634

635

636

637

638

639

640

641

642

643

644

645

646

Calculating slip

647

648

649

650

651

652

653

654

The second glaciologically important parameter to measure at the bed is the slip, and hence the basal slip-rate. To calculate slip, we assume that while an individual icequake cluster is active, all (or at least the vast majority of) slip is accommodated seismically. This is likely the case for RIS, as evidenced by the close agreement between surface slip-rate and seismically measured basal slip-rates (see Fig. 2f). Calculating the basal slip, d , from an icequake is challenging because one first has to determine a method of estimating the bed shear-modulus, G_{bed} , since the slip is given by,

655

$$d = \frac{M_0}{G_{bed} \cdot A} \quad (14),$$

656

where M_0 is the seismic moment released by an earthquake and A is the area of the fault.

657

658

659

660

661

662

663

664

665

666

667

The bed shear-modulus, G_{bed} , is calculated by assuming a further behavior of the rate- and state- friction law. This behavior is that an earthquake can only nucleate if it is in the unstable regime. In this study, we assume that the temporally-averaged driving shear-stress at the fault varies over longer time-scales than the icequake inter-event time, with the shear-stress at which the fault fails governed by the effective-normal-stress acting on the fault, $\bar{\sigma}$. The approximately constant inter-event time between individual consecutive icequake pairs (see Fig. 2e) within a single cluster validates this assumption.³¹ define the effective-normal-stress at which a fault becomes unstable is defined as the critical normal stress, $\bar{\sigma}_c$, with velocity-weakening behavior prevailing above this stress. $\bar{\sigma}_c$ is given by³¹,

668

$$\bar{\sigma}_c = \frac{k \mathcal{L}}{b-a} \quad (15),$$

669

where k is the spring constant of the system (see Extended Data Fig. 3a), which is given by,

670

671

$$k = \frac{G^*}{R} \quad (16),$$

672

where G^* is the effective shear-modulus of the bimaterial interface¹⁹ and R here is the radius of the fault, which can be found from the icequake corner frequency, if assuming a

673

674 symmetric, circular fault^{66,67}. However, this equation still has two unknowns: G^* , the
 675 effective shear-modulus that we require to calculate the slip; and \mathcal{L} , the critical slip
 676 distance, otherwise referred to as the state evolution distance. For the purposes of this
 677 study, we approximate \mathcal{L} to remain constant, but allow G^* to vary with effective-normal-
 678 stress, which from granular material theory⁷⁴ is assumed to take the generic empirical
 679 form,

$$680 \quad G^* = A \bar{\sigma}^n + C \quad (17),$$

681 where A , n and C are constants to invert for. We use a least squares approach to minimize
 682 the function,

$$683 \quad f(\bar{\sigma}_c, R, a, b, A, n, C, \mathcal{L}) = \ln\left(\frac{(A \bar{\sigma}_c^n + C) \mathcal{L}}{b - a}\right) - \ln(R \bar{\sigma}_c) \quad (18),$$

684 where $\bar{\sigma}_c$ and R vary for each icequake, and A , n , C and \mathcal{L} are varied to minimize the
 685 function. $\bar{\sigma}_c$ is taken to be the effective-normal-stress for the first 100 icequakes when a
 686 cluster becomes active, as calculated using Equation 13. These parameters are found to
 687 be $A = 22,000$, $n = 0.78$, $C = 8,200 \text{ Pa}$ and $\mathcal{L} = 7.7 \times 10^{-5} \text{ m}$, with the result of the
 688 minimization shown in Extended Data Fig. 4. Now \mathcal{L} can be substituted into Equation 15
 689 to find the bimaterial shear-modulus, G^* . The shear-modulus of the bed, G_{bed} can then be
 690 found using the Poisson ratios of ice (1/3) and till (0.49), which gives $G^* \approx 3.5 G_{bed}$ ¹⁹.
 691 Granular material theory, or at least the relationship of Equation 17, is thought to still
 692 hold for clast-over-bedrock sliding since the shear-modulus will still be related to some
 693 exponent, n , of $\bar{\sigma}$, even if that exponent were ~ 0 .
 694

695 Equation 14 can then be used to find the slip, d , associated with a single icequake, for the
 696 effective-normal-stress applied to the fault at that particular time. We also calculate the
 697 approximate slip-rate associated with these highly repetitive icequakes. If one assumes
 698 that all the slip when an icequake cluster is active is accommodated seismically, then one
 699 can calculate the slip-rate per day, v_{slip} ,

$$700 \quad v_{slip} = \frac{d}{t_{inter-event}} \quad (19),$$

701
 702 The methods described above allow us to calculate the total shear-stress, τ , and the slip,
 703 d , at the bed. These two parameters can provide observational constraint on ice dynamics
 704 models of ice streams.
 705

706 ***A note on assumptions***

707 A number of assumptions are made to make the derivation of basal shear-stress and slip from
 708 icequake observations and a rate-and-state friction model mathematically tractable. There are
 709 several assumptions that warrant particular emphasis. The first is the assumption that all slip at
 710 an individual sticky-spot is accommodated seismically while that cluster is active. The highly
 711 repetitive nature of the icequakes (see Extended Data Fig. 1 and²⁸), with approximately constant
 712 inter-event times between consecutive icequakes in a cluster, is indicative of the stability of each
 713 sticky-spot (see Fig. 2), justifying this assumption. Secondly, a Brune model⁶³ is assumed to
 714 describe the earthquake source characteristics. While such a model is likely an approximation for
 715 the complex physics of earthquake rupture, it is a common assumption for other earthquake
 716 studies that is likely also a valid approximation for the stick-slip icequakes presented here.
 717 Thirdly, we approximate that the time-derivative of the state-variable in the rate-and-state

718 friction model, $\frac{\partial \theta}{\partial t}$, equals zero during an individual icequake cycle. This approximation is valid
 719 if slip on the fault is sufficiently fast and if little damage occurs at the fault, compared to more
 720 complex earthquake faults. Obviously, this is only an approximation, as damage does likely
 721 occur at the fault, at least for the clasts-over-bedrock slip case (regime I, see Fig. 5).
 722 Furthermore, an underestimation bias in slip may be introduced by the assumption of no fault
 723 frictional heating. Fault frictional heating would reduce the seismic radiation efficiency from our
 724 approximation of one⁷². The final assumption we emphasize here is that we assume that the
 725 icequakes at the beginning of an icequake cluster nucleate at approximately the critical normal
 726 stress for nucleation, σ_c , rather than at some arbitrary value above it. The icequake slip
 727 calculations are dependent upon this assumption. This assumption would not be valid for
 728 sporadic earthquakes on complex faults, as shear-stresses could build to different values before
 729 failure for each earthquake, even with constant effective-normal-stresses, due to fault
 730 heterogeneity. Nor would it necessarily be valid if the driving shear-stress were perturbed over
 731 time-scales shorter than the inter-event time, for example by interactions with other icequake
 732 clusters. However, although icequake faults still exhibit a degree of heterogeneity due to an
 733 inhomogeneous distribution of clasts, this heterogeneity has negligible impact upon the
 734 consistency of both the inter-event times and shear-stresses between consecutive icequakes at a
 735 given sticky-spot (see Fig. 2). Furthermore, there are only a small number of active icequake
 736 clusters at any given time, which are spatially isolated from one another. The consistency in
 737 inter-event times and shear-stresses observed in our data, in agreement with similar, laboratory-
 738 generated icequakes¹², provides us with confidence in our assumption of icequakes nucleating at
 739 the critical nucleation stress, σ_c .

740 **Additional references:**

- 741 58. Kufner, S. et al. Microseismic icequake catalogue, Rutford ice stream (west Antarctica),
 742 November 2018 to February 2019 (version 1.0). UK Polar Data Centre, Nat. Environ. Res. Council.
 743 UK Res. Innov. (2021) doi:10.5285/B809A040-8305-4BC5-BAFF-76AA2B823734.
 744 59. Winder, T. et al. QuakeMigrate v1.0.0. Zenodo (2021) doi:10.5281/zenodo.4442749.
 745 60. Lomax, A. & Virieux, J. Probabilistic earthquake location in 3D and layered models. *Adv. Seism.*
 746 *Event Locat. Vol. 18 Ser. Mod. Approaches Geophys.* 101–134 (2000).
 747 61. Hudson, T. S. TomSHudson/SeisSrcMoment: First formal release (Version 1.0.0). Zenodo (2020)
 748 doi:http://doi.org/10.5281/zenodo.4010325.
 749 62. Aki, K. & Richards, P. G. *Quantitative Seismology*. (University Science Books, 2002).
 750 63. Brune, J. N. Tectonic Stress and the Spectra of Seismic Shear Waves from Earthquakes. *J.*
 751 *Geophys. Res.* 75, 4997–5009 (1970).
 752 64. Peters, L. E., Anandkrishnan, S., Alley, R. B. & Voigt, D. E. Seismic attenuation in glacial ice: A
 753 proxy for englacial temperature. *J. Geophys. Res. Earth Surf.* 117, 1–10 (2012).
 754 65. Madariaga, R. Dynamics of an expanding circular fault. *Bull. Seismol. Soc. Am.* 66, 639–666
 755 (1976).
 756 66. Kaneko, Y. & Shearer, P. M. Seismic source spectra and estimated stress drop derived from
 757 cohesive-zone models of circular subshear rupture. *Geophys. J. Int.* 197, 1002–1015 (2014).
 758 67. Kaneko, Y. & Shearer, P. M. Variability of seismic source spectra, estimated stress drop, and
 759 radiated energy, derived from cohesive-zone models of symmetrical and asymmetrical circular and
 760 elliptical ruptures. *J. Geophys. Res. Solid Earth* 120, 1053–1079 (2015).
 761 68. Eshelby, J. D. The determination of the elastic field of an ellipsoidal inclusion, and related
 762 problems. *Proc. R. Soc. London. Ser. A. Math. Phys. Sci.* 241, 376–396 (1957).
 763 69. Ruina, A. Slip instability and state variable friction laws. *J. Geophys. Res.* 88, 10359–10370
 764 (1983).
 765 70. Hanks, T. C. & McGuire, R. K. The character of high-frequency strong ground motion. *Bull.*
 766

- 767 Seismol. Soc. Am. 71, 2071–2095 (1981).
768 71. Dieterich, J. H. Time-dependent friction and the mechanics of stick-slip. *pure Appl. Geophys.* 116,
769 790–806 (1978).
770 72. Kanamori, H. & Rivera, L. Energy partitioning during an earthquake. in *Geophysical Monograph*
771 *Series vol. 170* 3–13 (2006).
772 73. Calderoni, G., Rovelli, A. & Di Giovambattista, R. Stress Drop, Apparent Stress, and Radiation
773 Efficiency of Clustered Earthquakes in the Nucleation Volume of the 6 April 2009, Mw 6.1
774 L’Aquila Earthquake. *J. Geophys. Res. Solid Earth* 124, 10360–10375 (2019).
775 74. Lade, P. V. & Nelson, R. B. Modelling the elastic behaviour of granular materials. *Int. J. Numer.*
776 *Anal. Methods Geomech.* 11, 521–542 (1987).
777 75. Weertman, J. On the Sliding of Glaciers. *J. Glaciol.* 3, 33–38 (1957).

778

779

780

781

782

783

784

785

786

787

788

789

790

791

792

793

794

795

796

797

798

799

800

801

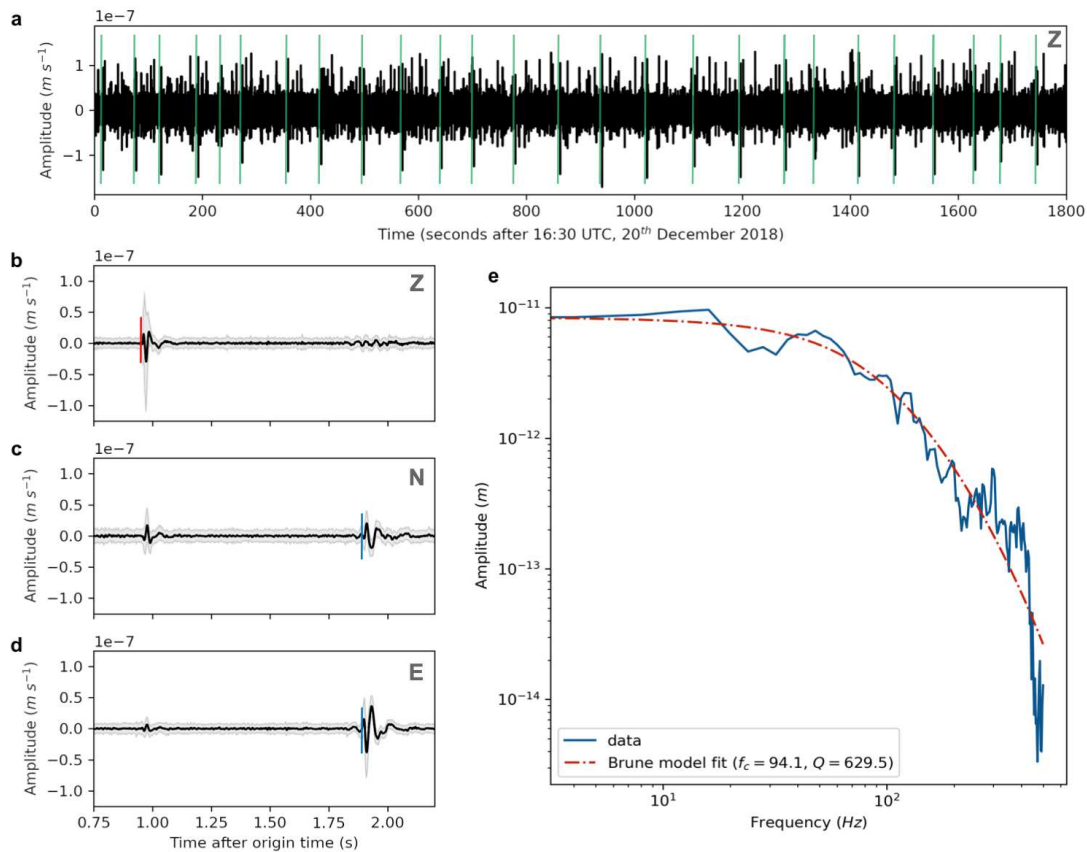
802

803

804

Extended Data Figures

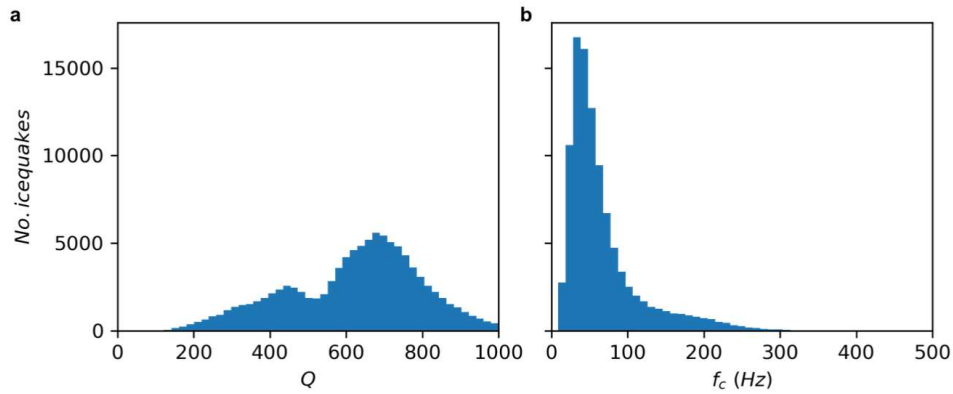
805



806

807 **Extended Data Fig. 1. Examples of icequake waveforms and spectra.** (a) 30 minutes of
 808 continuous data for the Z component of station R3030. Approximate icequake P-phase arrival
 809 times associated with a single cluster are shown by the green lines. (b), (c), (d) Stacked
 810 waveform data on the Z-, N- and E- components for 173 events in a cluster at station R3030,
 811 located at the center of the network. Red line indicates P-phase arrival. Blue lines indicate S-
 812 phase arrivals. Grey shading represents the standard deviation of the stacked data. (e) Spectrum
 813 for one event within the cluster at station R3030. Waveform data in (a) to (d) are filtered between
 814 10 Hz and 120 Hz.

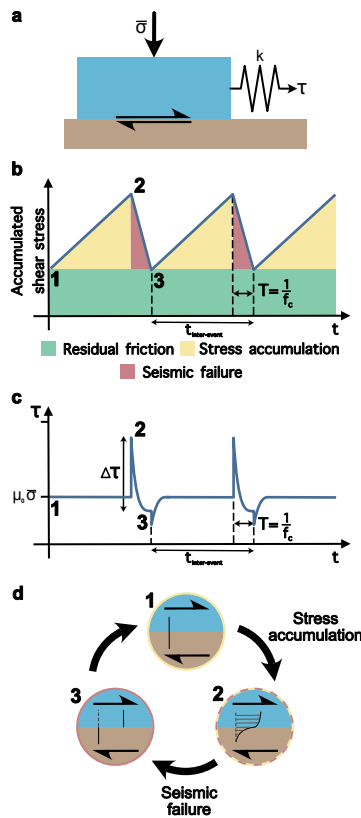
815



816

817 **Extended Data Fig. 2. Quality factor (Q) and corner frequency (f_c) distributions for the**
 818 **icequakes in this experiment. (a) Histogram of Q . (b) Histogram of f_c . Values for each**
 819 **icequake are averaged for all individual station observations.**

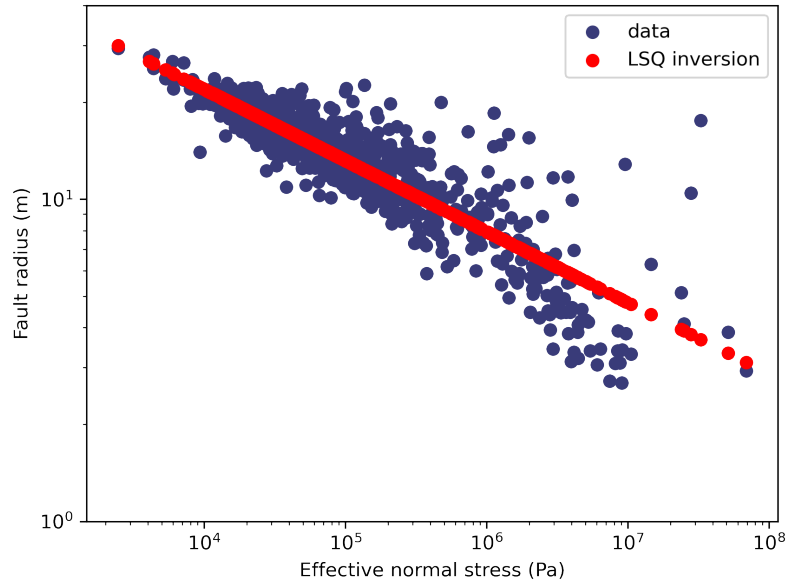
820



821

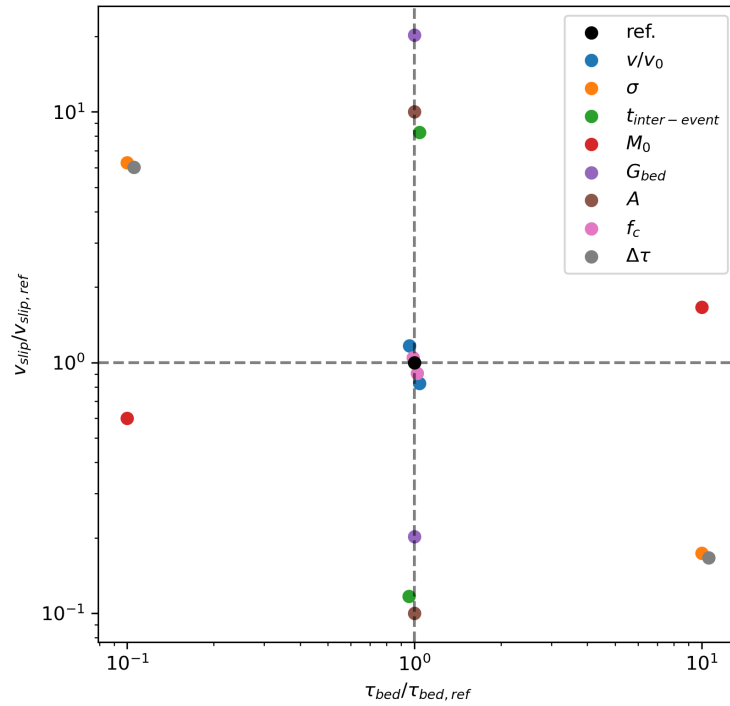
822 **Extended Data Fig. 3. Schematic Fig. describing the rate- and state- frictional model as a**
 823 **block-slider model. (a) Diagram of the block-slider model, showing the driving shear-stress, τ ,**
 824 **the effective-normal-stress, $\bar{\sigma}$, and the system spring constant k . (b) Accumulated shear-stress**
 825 **vs. time for a series of consecutive icequakes. (c) Shear-stress at the fault at a particular time as**

826 predicted by the rate-and-state model ³¹. (d) The stick-slip icequake cycle, with the numbers
 827 corresponding to the relevant stress states labelled in (b).
 828



829
 830 **Extended Data Fig. 4. Results of the least squares inversion of Equation 17.** Blue scatter
 831 points are the data and red scatter points show the least-squares inversion result.

832
 833
 834



835

836 **Extended Data Fig. 5. Rate-and-state friction model sensitivity analysis.** Plot of the
 837 sensitivity in frictional shear-stress at the bed, τ_{bed} , and slip-rate at the bed, v_{slip} , with
 838 perturbation of the key observational parameters. The reference values used to normalize the
 839 variations are the average values of τ_{bed} and v_{slip} observed at all the clusters. The magnitude of
 840 variation in each parameter are summarized in Table S1. See supplementary text for further
 841 details.

842

843

844

845

846

847

848

849

850

851

852

853

854

Supplementary Files

This is a list of supplementary files associated with this preprint. Click to download.

- [frictionandslipicequakespaperHudson2021supplementaryinformation.pdf](#)